

Optical Injection and Detection of Long-Lived Interlayer Excitons in van der Waals Heterostructures

Alperen Tüğen^{1,*}, Anna M. Seiler^{1,*}, Kenji Watanabe², Takashi Taniguchi³, Martin Kroner¹, and Ataç İmamoğlu¹

¹*Institute for Quantum Electronics, ETH Zurich, CH-8093 Zurich, Switzerland*

²*Research Center for Electronic and Optical Materials,
National Institute for Materials Science, Tsukuba, Japan and*

³*Research Center for Materials Nanoarchitectonics,
National Institute for Materials Science, Tsukuba, Japan*

(Dated: June 9, 2025)

Interlayer excitons in semiconducting bilayers separated by insulating hBN layers constitute a promising platform for investigation of strongly correlated bosonic phases. Here, we report an optical method for the generation and characterization of long-lived interlayer excitons. We find confirmation of tightly bound interlayer excitons by measuring 1s and 2s intralayer excitons in each layer concurrently. Using a pump-probe technique, we find interlayer exciton lifetimes up to 8.8 μs , increasing with the thickness of the hBN. With optical access to long-lived interlayer excitons, our approach provides a new promising route to explore degenerate Bose-Fermi mixtures of excitons and itinerant electrons with high spatial and temporal resolution.

Transition metal dichalcogenide (TMD) heterobilayers have recently emerged as a promising platform for creating long-lived interlayer excitons, bound electron-hole pairs, whose constituents reside in different layers. With their large binding energy and a built-in out-of-plane dipole, they offer a route to investigate many-body phenomena ranging from superfluidity of dipolar excitons [1–4] to Bose-Fermi mixtures exhibiting exotic electron pairing mechanisms [5, 6] in van der Waals heterostructures. However, accessing these collective states depends on controlling the lifetime, density, and interactions of interlayer excitons [3, 7].

Early demonstrations of long-lived interlayer excitons relied on the electrical injection of charge carriers into separate TMD layers [8–11]. Capacitance spectroscopy and Coulomb-drag measurements provided compelling evidence for interlayer exciton formation. While such measurements reveal static charge configurations, they offer limited information on time dynamics and spatial distributions. An alternative route that gives access to exciton dynamics employs non-resonant optical excitation of nearly aligned MoSe₂-WSe₂ bilayers, either in direct contact or separated by one or two hexagonal boron nitride (hBN) layers [12–15]. Photoluminescence (PL) from such devices has revealed interlayer exciton lifetimes up to 1.9 μs [16]. However, achieving longer interlayer exciton lifetimes and higher densities requires thicker hBN spacer layers to suppress residual interlayer tunneling and radiative recombination [17]. This, in turn, significantly reduces PL emission, rendering direct optical measurements of the interlayer exciton dynamics untenable.

Here, we demonstrate an optical scheme that overcomes the limitations of both electrical and PL-based injection and detection schemes. By inserting hBN spacer with up to seven layers to suppress interlayer tunnelling,

we inject high densities of electrons and holes into separate MoSe₂ and WSe₂ layers via non-resonant optical pumping, without requiring layer-selective contacts or complex gating geometries [8, 9]. Using time-resolved reflection spectroscopy and the 2s exciton resonance as a spectroscopic probe, we observe interlayer exciton formation and relaxation dynamics, in samples with negligible interlayer exciton-PL. Under these conditions, we achieve interlayer exciton densities up to $n_{\text{IX}} \approx 1 \times 10^{12} \text{ cm}^{-2}$ and lifetimes of 8.8 μs . This combination of high density, long lifetime, and optical control opens the door to studying strongly interacting interlayer exciton gases and exploring collective excitonic phenomena.

In this work, we investigate three different TMD bilayer devices with varying hBN spacer thicknesses (see Fig. 1a). In the main text, we present data from Devices 1 and 2, both MoSe₂-WSe₂ bilayers, while results from Device 3, a MoS₂-WSe₂ bilayer, are provided in the Supplemental Information (SI). Device 1 features a single-layer hBN spacer, Device 2 includes a 3–5 layer spacer, and Device 3 incorporates a 5–7 layer spacer. In contrast to the optical studies mentioned above, all TMD layers within a device are angle-misaligned, suppressing interlayer hybridization, and resulting in negligible interlayer PL [18]. A schematic of a typical device structure is shown in Fig. 1a, and optical micrographs along with fabrication details are available in the SI.

To determine the charge configuration in the individual layers, we perform reflection contrast spectroscopy. The upper panel of Fig. 1b shows spectra of the MoSe₂ and WSe₂ 1s exciton resonances as a function of the gate voltage V_{μ} (controls the chemical doping of the layers, see SI for details), measured in Device 1. Upon injection of itinerant charge carriers, the 1s exciton evolves into two distinct resonances: the repulsive polaron (RP) and the attractive polaron (AP) [19]. The left (right) side of the blue (red) dashed line in Fig. 1b corresponds to hole (electron) injection into the WSe₂ (MoSe₂) layer. The voltage range between the dashed lines marks the

* These authors contributed equally to this work.

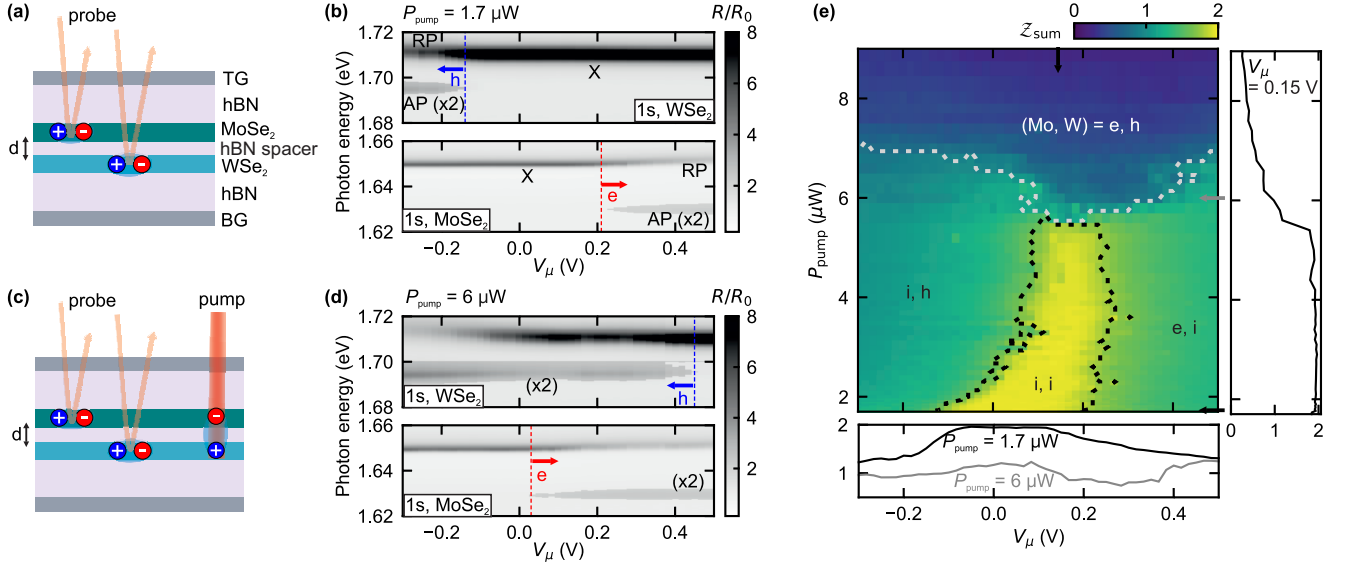


FIG. 1. (a) Schematic of the device structure. The thickness d of the spacer hBN layer varies between one and five layers depending on the specific device. Intralayer excitons are optically generated in both TMD layers and serve as probes of the device's charge configuration. (b) Normalized reflection spectra (R/R_0) of the MoSe₂ and WSe₂ layers as a function of gate voltage V_μ . Resonances corresponding to the repulsive polaron (RP), attractive polaron (AP), and neutral exciton (X) are indicated. Blue and red dashed lines mark the onset of hole and electron doping, respectively. A weak pump power was present during acquisition ($P_{\text{pump}} = 1.7 \mu\text{W}$); its effect on the spectra is negligible. (c) Schematic under pump-conditions. The pump locally injects carriers into the heterostructure, resulting in the generation of opposite charge carriers in the two layers. (d) R/R_0 at finite pump power ($P_{\text{pump}} = 6 \mu\text{W}$). Compared to (b), the onset voltages for electron and hole doping shift, and a new region emerges where electron and hole doping occur simultaneously. (e) The sum of the peak 1s X (RP) reflection contrasts of the MoSe₂ and WSe₂ layers, each normalized to its respective reflection contrast in the absence of charges, Z_{sum} , is shown as a function of gate voltage V_μ and pump power P_{pump} . Distinct charge configurations are labeled as (i, i), (i, h), (e, i), and (h, e), representing combinations of intrinsic (i), hole (h), and electron (e) doping in the Mo and W layers, respectively. The dotted black contour marks the region where the normalized X (RP) reflection contrast in both layers exceeds 0.7, indicating approximate charge neutrality; note, however, that small but finite doping persists near the boundary of the (i, i) region. The dotted light grey contour outlines the region with opposite doping in the two layers, where the normalized X (RP) reflection contrast in each layer falls below 0.7. Arrows indicate the positions of vertical and horizontal linecuts. Data in panels (b)–(e) were acquired using Device 1.

charge-neutral regime, where neither layer is doped.

MoSe₂–WSe₂ heterobilayers feature a type-II band alignment with an interlayer gap of approximately 1.6 eV [20]. Bridging this energy offset across even a few layers of hBN would require an out-of-plane electric field that exceeds the dielectric breakdown strength of hBN in the perpendicular direction [21]. Previous approaches to simultaneously dope both layers with opposite charges have relied on applying a finite interlayer bias to effectively reduce the band offset [8–11]. In our experiments, we employ electrical gates and non-resonant optical pumping to inject charge carriers into the TMD bilayer. We illuminate the sample with continuous-wave laser light at 635 nm, above the bandgap, as schematically illustrated in Fig. 1c. Remarkably, as we show below and in the SI, this optical doping technique enables simultaneous electron- and hole-doping in opposite layers even for devices with thicker hBN spacers, overcoming the intrinsic band-offset limitations without the need for applying an electrical bias.

Fig. 1d displays the reflection spectra measured in De-

vice 1 under continuous non-resonant pumping at laser power $P_{\text{pump}} = 6 \mu\text{W}$. Under these illumination conditions, the charge-neutral region observed in Fig. 1b vanishes, and we observe simultaneous electron doping in the MoSe₂ layer and hole doping in the WSe₂ layer. This is indicated by the reversal in the positions of the red and blue dashed lines. We emphasize that the two types of doping can be spectrally distinguished in WSe₂ [22]: the presence of a single attractive polaron (AP) resonance in the WSe₂ spectrum unequivocally indicates hole doping, since electron doping of WSe₂ leads to two AP features associated with the singlet and triplet trions [23].

To visualize the overall charge configuration, Fig. 1e shows the sum of the peak 1s X (RP) reflection contrast of MoSe₂ and WSe₂ layers normalized to the individual reflection contrast of each layer in the absence of charges (Z_{sum}) as a function of V_μ and P_{pump} (see SI for details). The yellow region labeled as (i,i) and outlined by a black-dotted contour, denotes the charge-neutral regime, where both excitons reach maximum contrast; we note that small but finite doping persists near the boundaries

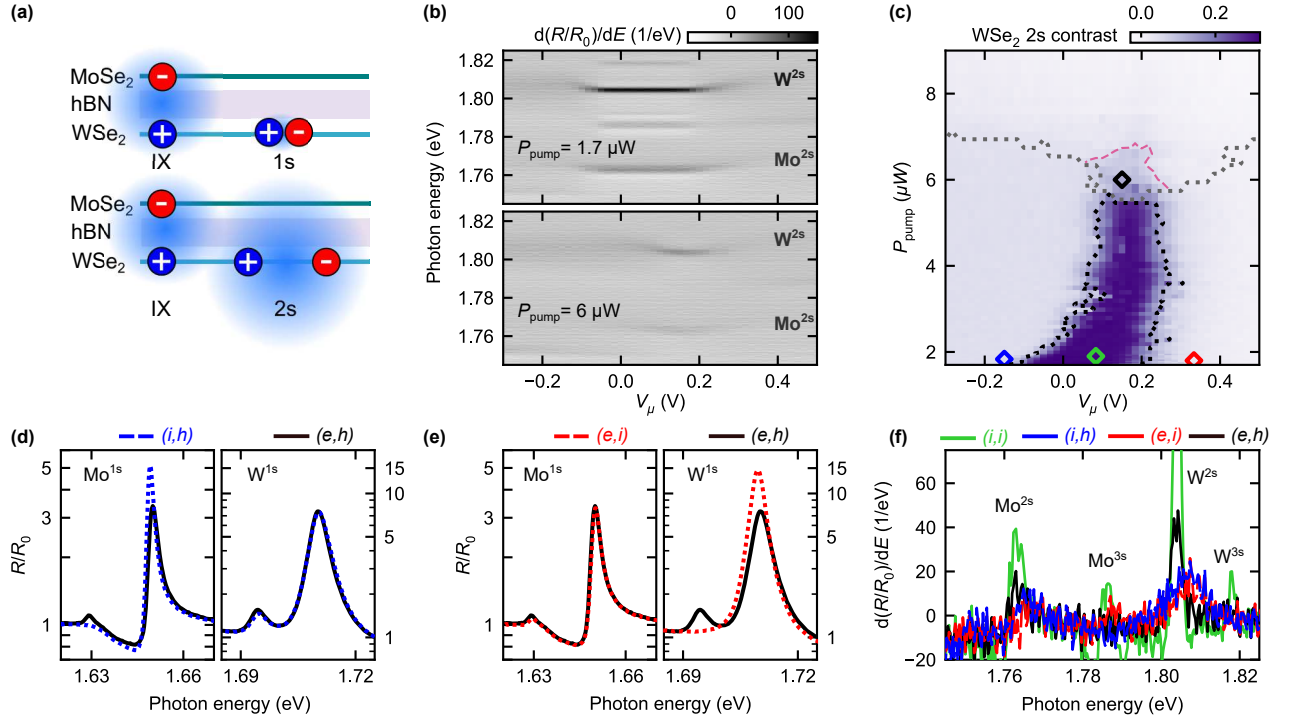


FIG. 2. (a) Schematic illustration of the spatial extent of 1s, 2s intralayer excitons and interlayer exciton (IX). (b) Differential reflection spectra ($d(R/R_0)/dE$) plotted as a function of gate voltage V_μ , in the energy range corresponding to the Rydberg exciton resonances. Data are shown for pump powers of $P_{\text{pump}} = 1.7 \mu\text{W}$ (upper panel) and $P_{\text{pump}} = 6 \mu\text{W}$ (lower panel). MoSe₂ and WSe₂ 2s Rydberg resonances are labeled, the 3s Rydberg resonances are discussed in the SI (Fig. S7). (c) Colormap of WSe₂ 2s contrast as a function of gate voltage V_μ and pump power P_{pump} . The dashed black and grey contour lines delineate different charge configurations, defined as in Fig. 1e. The dashed pink contour marks the boundary where the WSe₂ 2s contrast falls below 0.055 (20%) in the region where the two layers are oppositely doped. (d,e) Log-scale spectral linecuts illustrating distinct doping configurations. The blue and red curves correspond to only hole doping in WSe₂ and only electron doping in MoSe₂, respectively, with the opposite layer remaining charge neutral. The black curve shows simultaneous doping of both layers, with individual charge carrier densities matching those in the red and blue cases. V_μ and P_{pump} settings for each linecut are indicated in panel (c) by color-coded diamond markers. (f) Differential reflection spectra ($d(R/R_0)/dE$) plotted over the energy range corresponding to the Rydberg exciton resonances. The green curve, measured at charge neutrality (see green diamond in panel (c)), shows the bare Rydberg excitons. The 2s resonance disappears when only one layer is doped (red and blue curves), but remains visible without a significant spectral shift when both layers are doped simultaneously (black curve). Data in panels (b)–(f) were acquired using Device 1.

of this region. At higher pump powers, a dark blue region appears above a light gray dotted contour line, indicating dual-layer doping with opposite charge carriers (e,h). In the surrounding regions, either WSe₂ is hole doped (i,h) or MoSe₂ is electron doped (e,i), with the opposite layer remaining charge neutral. The absence of sharp vertical boundaries at fixed V_μ in the charge-neutral region (see the curved shape of the black contour in Fig. 1e) reflects the non-equilibrium nature of the charge distribution. This suggests that optical pumping may lead to excess hole generation in the WSe₂ layer.

Having established the charging configuration in both layers, we investigate whether the injected electrons and holes form bound interlayer exciton states, or remain unbound. Prior theoretical work [9, 24] demonstrated that the modification of the 1s exciton-polaron resonances can be used to differentiate between bound and unbound interlayer electron-hole pairs: however, the associated spec-

tral shifts are rather small and can be masked by exciton line broadening. The origin of this relatively weak dependence is the small Bohr radius of 1s intralayer excitons, rendering them insensitive to the charges in the neighboring TMD layer (see the sketch in the upper panel of Fig. 2a). In contrast, Rydberg exciton states, such as the 2s state, exhibit a significantly larger Bohr radius (lower panel of Fig. 2a), making them more sensitive to the surrounding electrostatic environment [25]. As such, the 2s exciton reflection contrast can be expected to respond differently depending on whether the charge carriers are (tightly) bound as interlayer excitons or remain free unbound particles.

As shown in the upper panel of Fig. 2b, we can clearly resolve MoSe₂ and WSe₂ 2s and 3s excitons in the charge-neutral regime. In the case of free carriers residing in the same layer, 2s excitons exhibit a blue shift and loss of oscillator strength even for small carrier densities. In

contrast, when charges are located in the opposite layer, the 2s excitons experience a large redshift [25–27]. Interestingly, we observe that in the regime where both layers are doped under finite pump power, the MoSe₂ and WSe₂ 2s exciton features persist with reduced intensity but exhibit no spectral shift (lower panel of Fig. 2b). To systematically quantify this behavior across the charge map, we extract the WSe₂ 2s contrast, defined as the peak-to-peak amplitude of the dispersive Lorentzian lineshape associated with the WSe₂ 2s exciton (Fig. 2c). In Figs. 2d–f, we show differentiated spectral line cuts corresponding to the selected points in the phase diagram marked with diamonds. Notably, the 2s exciton contrast remains finite within the region of dual-layer doping marked by the black diamond, even though the charge densities in each layer are comparable to those in the red and blue diamond regions, where the 2s resonance is absent. Furthermore, the spectral position of the 2s resonance in the black diamond region coincides with that in the green diamond region of Fig. 2c, corresponding to the regime where both layers are charge neutral. This spectral stability in the presence of dual-layer doping stands in stark contrast to the drastic modification of 2s resonances due to free charges in either layer, and points to a distinct, underlying phase consistent with the formation of interlayer excitons. We further observe that the 2s exciton

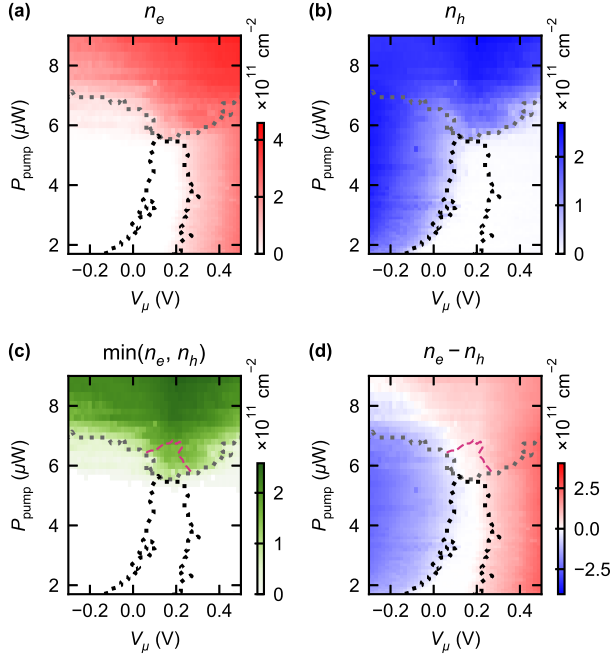


FIG. 3. Charge carrier densities extracted from the optical spectra measured in Device 1 as a function of the gate voltage, V_μ , and pump power, P_{pump} : (a) electron density, n_e , in the MoSe₂ layer; (b) hole density, n_h , in the WSe₂ layer; (c) minimum of n_e and n_h ($\min(n_e, n_h)$); (d) excess charge $n_e - n_h$. Dotted contour lines denote the same boundaries depicted in Figs. 1e and 2c.

contrast diminishes progressively with increasing pump power; the dashed pink line in Fig. 2c) delineates the boundary where the WSe₂ 2s contrast falls below 20% of its original value. This behavior is expected: as the average interlayer exciton spacing decreases and eventually approaches the 2s exciton Bohr radius, the 2s excitons interacting with interlayer excitons will be more effectively screened. Concurrently, increasing the Bohr radius of the interlayer excitons will also enhance the screening of 2s excitons. The fact that 3s exciton resonance vanishes at even lower interlayer exciton densities supports our explanation (Fig. S7).

We extract electron and hole densities (n_e and n_h) from the 1s exciton–polaron spectrum. In the absence of optical pumping, integer quantum Hall states under high magnetic field establish a mapping between V_μ and charge carrier density [28] (Fig. S8). We then use the charge carrier density-dependent AP and RP amplitudes for a given V_μ to provide a spectral measure for the charge carrier density. Under optical pumping, this mapping allows direct inference of n_e and n_h from the measured polaron resonances across the entire $V_\mu - P_{\text{pump}}$ map (Fig. S9, see SI for more information).

In Figs. 3a,b, we show the resulting maps of n_e and n_h as functions of V_μ and P_{pump} . From these, we extract the minimum of (n_e, n_h) ($\min(n_e, n_h)$) and the excess charge density, shown in Figs. 3c,d. The excess charge is defined as $n_e - n_h$, while $\min(n_e, n_h)$ provides an upper bound on the attainable interlayer exciton density. In particular, the excess charge is minimal in the regime where both layers are doped, and yet the 2s resonance remains visible (see black diamond marker), corroborating the presence of bound electron–hole pairs.

Figures 3a and 3b show maps of the electron and hole densities, n_e and n_h , as functions of V_μ and P_{pump} , from

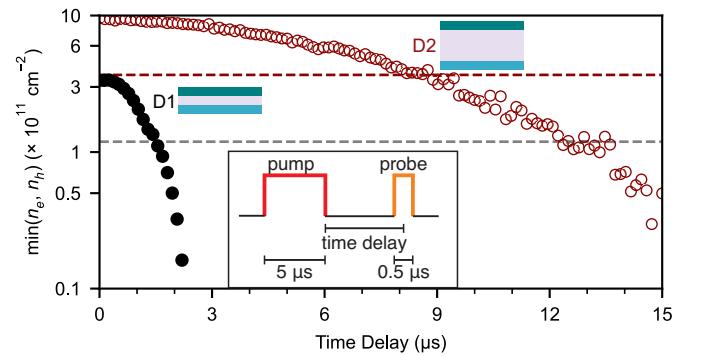


FIG. 4. Time evolution of the minimum of the electron and hole densities, $\min(n_e, n_h)$, as a function of time delay between the pump and probe pulses (see inset). Data points from Device 1 (D1, monolayer hBN spacer) are shown as black filled circles, while those from Device 2 (D2, 3–5-layer hBN spacer) are shown as dark red open circles. The dashed lines mark the density at which $\min(n_e, n_h)$ has decayed to $1/e$ of its initial value; the corresponding delay times are 1.4 μs for Device 1 and 8.8 μs for Device 2.

which we extract the minimum of (n_e, n_h) ($\min(n_e, n_h)$) and the excess charge density $n_e - n_h$, plotted in Figures 3c and 3d. Within the region enclosed by the pink dashed contour, the 2s contrast is visible and coincides with the region where the excess charge approaches zero, confirming that the carriers are paired and thus form interlayer excitons. In this regime, the interlayer exciton density is set by $\min(n_e, n_h)$. Outside the pink contour, interlayer excitons may still be present alongside free carriers, but the 2s spectroscopic signature lacks sufficient contrast to confirm their presence. Here, $\min(n_e, n_h)$ provides an upper bound on the attainable interlayer exciton density. In Device 1, where the MoSe₂ and WSe₂ layers are separated by a monolayer of hBN, the $\min(n_e, n_h)$ reaches up to $3 \times 10^{11} \text{ cm}^{-2}$. By contrast, in Device 2, which features an hBN spacer thickness of 3–5 layers, $\min(n_e, n_h)$ is significantly higher and reaches $1 \times 10^{12} \text{ cm}^{-2}$ (Fig. S10).

The optical pumping scheme we employ in our experiments provides access to interlayer exciton dynamics. We probe these dynamics using time-resolved reflection spectroscopy, with synchronized modulation of the pump and probe beams that allows for programmable delays between pulses (see SI for details). In Fig. 4, we present the evolution of $\min(n_e, n_h)$ on a logarithmic scale as a function of pump–probe delay, enabling us to quantify the lifetime of the interlayer exciton state at a representative point in the phase diagram, where $\min(n_e, n_h)$ is finite, the total excess charge is negligible, and the WSe₂ 2s exciton is present. The decay of the $\min(n_e, n_h)$ signal with increasing time delay reflects the relaxation of interlayer excitons after the pump laser is turned off.

Even though the decay is clearly non-exponential, we extract an $1/e$ lifetime of $1.4 \mu\text{s}$ for Device 1 which contains a monolayer hBN spacer. In contrast, a significantly longer lifetime of $8.8 \mu\text{s}$ is observed for Device 2, which has a thicker hBN spacer of 5–7 layers. This prolonged lifetime is consistent with expectations: increased spacer thickness suppresses interlayer tunneling and reduces the radiative decay rate, thereby extending the interlayer exciton lifetime [16].

Surprisingly, the decay becomes faster at lower carrier densities [29]. We speculate that the shortened lifetime may stem from interlayer excitons becoming more tightly

bound as their density is lowered: Since the radiative decay rate scales inversely with the square of the Bohr radius, we would expect the lifetime to become shorter. Last but not least, we emphasize that our measurements cannot rule out a dominant, sample-dependent, nonradiative decay mechanism.

In summary, we present an all-optical method to generate and probe long-lived interlayer excitons in TMD heterobilayers with few-layer hBN spacers, where PL is strongly suppressed. Using time-resolved reflection spectroscopy, we measure exciton lifetimes up to $8.8 \mu\text{s}$ and a steady-state exciton density of $1 \times 10^{12} \text{ cm}^{-2}$. The generation of interlayer excitons within a focused optical spot, combined with the ability to probe their dynamics on picosecond timescales [30], provides a powerful platform for exploring degenerate dipolar excitons with high spatial and temporal resolution. Crucially, it allows spatially controlled exciton generation without the need for external electric fields, which are typically required in schemes requiring bias voltage for interlayer exciton generation [8, 9]. This capability opens the door to creating multiple excitonic reservoirs within a single device, paving the way for Josephson-like experiments [31–33]. In particular, optically inducing high-density exciton populations in two gate-defined traps [34, 35] connected by a narrow channel could provide a direct route to optically probing [36] coherent tunneling and phase dynamics between condensate regions.

ACKNOWLEDGMENTS

We thank Xiaobo Lu for fabricating Device 1. We thank Ivan Amelio, Haydn S. Adlong, Arthur Christensen and Igor Khanonkin for inspiring discussions. This work was supported by the Swiss National Science Foundation (SNSF) under Grant No. 200021-204076. A. M. S. acknowledges funding from an ETH Postdoctoral Fellowship. K.W. and T.T. acknowledge support from the JSPS KAKENHI (Grant Numbers 21H05233 and 23H02052), the CREST (JPMJCR24A5), JST and World Premier International Research Center Initiative (WPI), MEXT, Japan.

-
- [1] M. Lu, N. Q. Burdick, S. H. Youn, and B. L. Lev, *Phys. Rev. Lett.* **107**, 190401 (2011).
 - [2] K. Aikawa, A. Frisch, M. Mark, S. Baier, A. Rietzler, R. Grimm, and F. Ferlaino, *Phys. Rev. Lett.* **108**, 210401 (2012).
 - [3] M. Alloing, M. Beian, M. Lewenstein, D. Fuster, Y. González, L. González, R. Combescot, M. Combescot, and F. Dubin, *EPL* **107**, 10012 (2014).
 - [4] M. Combescot, R. Combescot, and F. Dubin, *Reports on Progress in Physics* **80**, 066501 (2017).
 - [5] C. Zerba, C. Kuhlenkamp, A. Imamoğlu, and M. Knap,

- Phys. Rev. Lett.* **133**, 056902 (2024).
- [6] J. von Milczewski, X. Chen, A. Imamoglu, and R. Schmidt, *Phys. Rev. Lett.* **133**, 226903 (2024).
- [7] A. A. High, J. R. Leonard, A. T. Hammack, M. M. Fogler, L. V. Butov, A. V. Kavokin, K. L. Campman, and A. C. Gossard, *Nature* **483**, 584 (2012).
- [8] L. Ma, P. X. Nguyen, Z. Wang, Y. Zeng, K. Watanabe, T. Taniguchi, A. H. MacDonald, K. F. Mak, and J. Shan, *Nature* **598**, 585 (2021).
- [9] R. Qi, A. Y. Joe, Z. Zhang, Y. Zeng, T. Zheng, Q. Feng, J. Xie, E. Regan, Z. Lu, T. Taniguchi, K. Watanabe,

- S. Tongay, M. F. Crommie, A. H. MacDonald, and F. Wang, *Nat. Commun.* **14**, 8264 (2023).
- [10] P. X. Nguyen, L. Ma, R. Chaturvedi, K. Watanabe, T. Taniguchi, J. Shan, and K. F. Mak, *Science* **388**, 274 (2025).
- [11] R. Qi, A. Y. Joe, Z. Zhang, J. Xie, Q. Feng, Z. Lu, Z. Wang, T. Taniguchi, K. Watanabe, S. Tongay, and F. Wang, *Science* **388**, 278 (2025).
- [12] P. Rivera, J. R. Schaibley, A. M. Jones, J. S. Ross, S. Wu, G. Aivazian, P. Klement, K. Seyler, G. Clark, N. J. Ghimire, *et al.*, *Nat. Commun.* **6**, 6242 (2015).
- [13] L. A. Jauregui, A. Y. Joe, K. Pistunova, D. S. Wild, A. A. High, Y. Zhou, G. Scuri, K. De Greve, A. Sushko, C.-H. Yu, *et al.*, *Science* **366**, 870 (2019).
- [14] Y. Shimazaki, I. Schwartz, K. Watanabe, T. Taniguchi, M. Kroner, and A. Imamoglu, *Nature* **580**, 472 (2020).
- [15] F. Mahdikhany, S. Arve Jahany, D. N. Shanks, M. Klein, Q. Wang, M. R. Koehler, D. G. Mandrus, T. Taniguchi, K. Watanabe, O. L. Monti, B. J. LeRoy, *et al.*, *Nat. Commun.* **13**, 5354 (2022).
- [16] J. Cutshall, F. Mahdikhany, A. Roche, D. N. Shanks, M. R. Koehler, D. G. Mandrus, T. Taniguchi, K. Watanabe, Q. Zhu, B. J. LeRoy, *et al.*, *Sci. Adv.* **11**, eadr1772 (2025).
- [17] D. Snoke, *Advances in condensed matter physics* **2011**, 938609 (2011).
- [18] Device 1 shows very weak interlayer PL, whereas no interlayer PL is observed in Devices 2 and 3; see Fig. S2.
- [19] M. Sidler, P. Back, O. Cotlet, A. Srivastava, T. Fink, M. Kroner, E. Demler, and A. Imamoglu, *Nat. Phys.* **13**, 255 (2017).
- [20] J. Kang, S. Tongay, J. Zhou, J. Li, and J. Wu, *Appl. Phys. Lett.* **102**, 012111 (2013).
- [21] Y. Hattori, T. Taniguchi, K. Watanabe, and K. Nagashio, *ACS Appl. Mater. Interfaces* **8**, 27877 (2016).
- [22] T. Wang, Z. Li, Z. Lu, Y. Li, S. Miao, Z. Lian, Y. Meng, M. Blei, T. Taniguchi, K. Watanabe, *et al.*, *Phys. Rev. X* **10**, 021024 (2020).
- [23] In contrast, MoSe₂ displays a single AP peak under both electron and hole doping, making carrier-type identification more ambiguous. Additional confirmation comes from Device 3, a MoS₂/WSe₂ heterostructure, where the MoS₂ layer clearly exhibits two AP features under electron doping, consistent with our interpretation of the spectra in Devices 1 and 2 (see Fig. S6).
- [24] I. Amelio, N. D. Drummond, E. Demler, R. Schmidt, and A. Imamoglu, *Phys. Rev. B* **107**, 155303, publisher: American Physical Society.
- [25] Y. Xu, S. Liu, D. A. Rhodes, K. Watanabe, T. Taniguchi, J. Hone, V. Elser, K. F. Mak, and J. Shan, *Nature* **587**, 214 (2020).
- [26] A. Popert, Y. Shimazaki, M. Kroner, K. Watanabe, T. Taniguchi, A. Imamoglu, and T. Smoleński, *Nano Lett.* **22**, 7363 (2022).
- [27] J. Kim, H. Dery, and D. Van Tuan, arXiv preprint arXiv:2505.06984 (2025).
- [28] T. Smoleński, O. Cotlet, A. Popert, P. Back, Y. Shimazaki, P. Knüppel, N. Dietler, T. Taniguchi, K. Watanabe, M. Kroner, *et al.*, *Phys. Rev. Lett.* **123**, 097403 (2019).
- [29] The parabolic trend in the logarithmic plot in Fig. 4 is clearly visible; similar non-exponential time dependence has also been observed by Cutshall *et al.* [16] in a time-resolved PL measurement.
- [30] T. Uto, B. Evrard, K. Watanabe, T. Taniguchi, M. Kroner, and A. Imamoglu, *Physical Review Letters* **132**, 056901 (2024).
- [31] B. Khorana, *Physical Review* **185**, 299 (1969).
- [32] F. Pascucci, S. Conti, D. Neilson, J. Tempere, and A. Perali, *Physical Review B* **106**, L220503 (2022).
- [33] G. Biagioni, N. Antolini, B. Donelli, L. Pezzè, A. Smerzi, M. Fattori, A. Fioretti, C. Gabbanini, M. Inguscio, L. Tanzi, *et al.*, *Nature* **629**, 773 (2024).
- [34] R. Rapaport, G. Chen, S. Simon, O. Mitrofanov, L. Pfeiffer, and P. Platzman, *Physical Review B—Condensed Matter and Materials Physics* **72**, 075428 (2005).
- [35] A. Gärtner, L. Prechtel, D. Schuh, A. Holleitner, and J. Kotthaus, *Physical Review B—Condensed Matter and Materials Physics* **76**, 085304 (2007).
- [36] E. C. Regan, D. Wang, C. Jin, M. I. Bakti Utama, B. Gao, X. Wei, S. Zhao, W. Zhao, Z. Zhang, K. Yumigeta, *et al.*, *Nature* **579**, 359 (2020).